

Highly sensitive gas refractometers based on optical microfiber modal interferometers operating at dispersion turning point

Zhang, Nancy Meng Ying; Li, Kaiwei; Zhang, Nan; Zheng, Yu; Zhang, Ting; Qi, Miao; Shum, Ping; Wei, Lei

2018

Zhang, N. M. Y., Li, K., Zhang, N., Zheng, Y., Zhang, T., Qi, M., . . . Wei, L. (2018). Highly sensitive gas refractometers based on optical microfiber modal interferometers operating at dispersion turning point. *Optics Express*, 26(22), 29148-29158. doi:10.1364/OE.26.029148

<https://hdl.handle.net/10356/81705>

<https://doi.org/10.1364/OE.26.029148>

© 2018 Optical Society of America under the terms of the OSA Open Access Publishing Agreement. Users may use, reuse, and build upon the article, or use the article for text or data mining, so long as such uses are for non-commercial purposes and appropriate attribution is maintained. All other rights are reserved.

Downloaded on 13 Mar 2024 17:39:14 SGT



Highly sensitive gas refractometers based on optical microfiber modal interferometers operating at dispersion turning point

NANCY MENG YING ZHANG,^{1,2} KAIWEI LI,^{1,3} NAN ZHANG,^{1,2} YU ZHENG,^{1,2} TING ZHANG,¹ MIAO QI,¹ PING SHUM,^{1,2} AND LEI WEI^{1,2,*}

¹*School of Electrical and Electronic Engineering, Nanyang Technological University, 50 Nanyang Avenue 639798, Singapore*

²*CINTRA CNRS/NTU/THALES, UMI3288, Research Techno Plaza, 50 Nanyang Drive 637553, Singapore*

³*likaiwei11@163.com*

**wei.lei@ntu.edu.sg*

Abstract: In most fiber-optic gas sensing applications where the interested refractive index (RI) is ~ 1.0 , the sensitivities are greatly constrained by the large mismatch between the effective RI of the guided mode and the RI of the surrounding gaseous medium. This fundamental challenge necessitates the development of a promising fiber-optic sensing mechanism with the outstanding RI sensitivity to achieve reliable remote gas sensors. In this work, we report a highly sensitive gas refractometer based on a tapered optical microfiber modal interferometer working at the dispersion turning point (DTP). First, we theoretically analyze the essential conditions to achieve the DTP, the spectral characteristics, and the sensing performance at the DTP. Results show that nonadiabatic tapered optical microfibers with diameters of 1.8–2.4 μm possess the DTPs in the near-infrared range and the RI sensitivities can be improved significantly around the DTPs. Second, we experimentally verify the ultrahigh RI sensitivity around the DTP using a nonadiabatic tapered optical microfiber with a waist diameter of $\sim 2 \mu\text{m}$. The experimental observations match well with the simulation results and our proposed gas refractometer provides an exceptional sensitivity as high as $-69984.3 \pm 2363.3 \text{ nm/RIU}$.

© 2018 Optical Society of America under the terms of the [OSA Open Access Publishing Agreement](#)

1. Introduction

Reliable gas sensors with high sensitivity, accuracy, portability and cost-effectiveness are widely demanded in real-world applications, including pressure or leak detections in industrial surveillance [1], discrimination of toxic and biological threats in environment monitoring [2], clinical diagnosis from exhaled breath [3], etc. Over the past two decades, optical fibers have been the prevailing gas sensing platforms benefited from their acute response, small footprint, flexibility, immunity to electromagnetic interference and remote sensing capability [4]. Numerous fiber-optic sensing mechanisms have been proposed for gas detections, of which the great majority can be classified into two categories, interferometry [5] and absorption spectroscopy [6]. Compared with absorption spectroscopy where the fingerprints of most gases fall within the mid-infrared range, interferometry based gas sensors are accessible for the well-developed near-infrared communication network with merits of high integration, cost effectiveness and remote monitoring. Thus, in this study, we mainly focus on fiber-optic interferometry based gas sensors, which are realized by measuring the refractive index (RI) of the gaseous sample [6–9]. Fiber-optic gas refractometers can be further classified into two operating principles: the evanescent wave (EW) based sensing and the open-cavity based sensing. The EW based gas RI sensors are mainly implemented by side-polished optical fibers, tapered optical fibers, optical fiber gratings, photonic crystal fibers (PCFs), etc [10–17]. However, the penetration depth of EW is greatly constrained due

to the large mismatch between the effective refractive indices (ERIs) of guided modes in optical fiber (~ 1.45) and the RI of gaseous medium (~ 1.0), resulting in weakened light-matter interaction thereby unpromising RI sensitivities. Hence, the sensitivities of EW based gas RI sensors can hardly break the ceiling of a few thousands of nanometers per refractive index unit (RIU) [18]. Also, open cavity based fiber-optic Fabry-Pérot interferometers (FPIs) and Mach-Zehnder interferometers have been intensively studied for gas sensing [19,20], yet most of them offer no breakthrough performance. One study of FPI based on PCF and the Vernier effect has successfully promoted the RI sensitivity in gaseous medium to the 10^4 nm/RIU level [21], however the complicated configuration of FPI limits the practical implementation and yield.

To address the aforementioned challenges, an optical microfiber modal interferometer operating at the dispersion turning point (DTP) is expected to be a promising solution. The DTP, which is also known as the critical point, was first discovered in a tapered optical fiber [22]. Later, researchers also observed the similar points in long-period fiber gratings [23,24] and few-mode optical fibers [25–27], and these sensors with DTPs can offer superior sensing performance, compared to their counterparts without the DTPs. A recent study numerically proved that tapered multimode optical microfiber with the DTP could provide ultrahigh RI sensitivity [28]. In our recent studies, we further showed that the DTPs in optical micro/nanofiber couplers were obtained across a broad surrounding refractive index (SRI) range of 1.0–1.41 by carefully designing the coupler's geometric parameters [18,29,30]. And we also experimentally demonstrated ultrahigh RI sensitivities exceeding 5×10^4 nm/RIU in different media using the DTPs in optical micro/nanofiber couplers.

Compared with the optical nanofiber coupler based sensors, the tapered optical microfiber is simpler in configuration and easier to fabricate, while providing a huge advantage in terms of sensitivity. However, the RI sensing potential of microfiber based modal interferometers especially for gaseous medium remains unexplored. Moreover, there is a lack in how to tailor the structural parameters so as to experimentally achieve the DTP in tapered optical microfiber modal interferometers. Therefore, in this work, we explore the RI sensing properties of tapered optical microfiber modal interferometers in gaseous medium. First, we theoretically optimize the diameter of the microfiber to match the SRI of gaseous medium. Then, we theoretically explore the influences of both the lengths of the transition regions and the length of the waist region on the position of the DTP. Guided by theoretical and numerical analysis, we properly design the structural parameters of tapered optical microfiber and experimentally realize the exceptional gas RI sensing performance of -69984.3 ± 2363.3 nm/RIU.

2. Theory and simulation

2.1 General expression for RI sensitivity of ideal uniform microfiber

Figure 1(a) illustrates the design of our proposed tapered optical microfiber modal interferometer for gas RI sensing. In a nonadiabatic optical microfiber tapered from a standard single-mode fiber (SMF), a uniform waist region is connected with the untapered regions through two abrupt transition regions. The fundamental LP_{01} core mode propagating in the untapered region can excite both the fundamental HE_{11} mode and the higher order HE_{12} mode in the transition taper. These two modes propagate through the uniform waist region and recombine in another transition taper. The beating between these two modes occurs when they travel along the tapered regions and the waist region. Due to the thin diameter of microfiber waist, the evanescent field of the excited modes leaks out of the microfiber and interacts with the ambient gas molecules. There, the change of surrounding gaseous medium would vary the optical path difference between the two modes, inducing altered interfering spectrum. The mode profiles of HE_{11} mode and HE_{12} mode for a 2 μm -thick microfiber at 1550 nm are presented in Fig. 1(b). It is obvious that most of the guided power is confined in

microfiber, and the HE_{12} mode has a substantial portion of the guided power in the form of EW. Thus, the HE_{12} mode is more sensitive to the change of the surrounding medium.

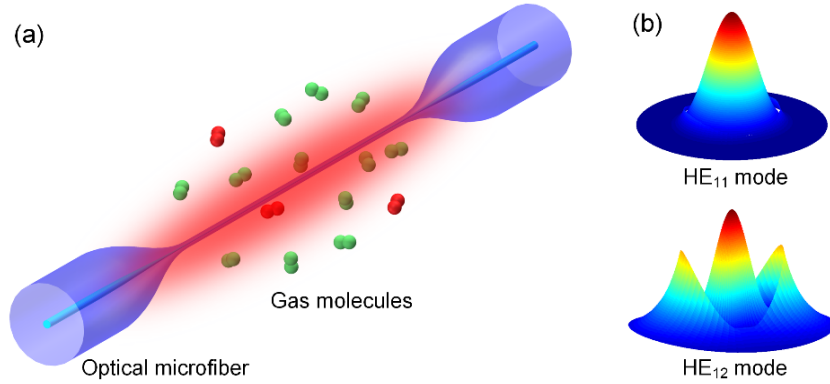


Fig. 1. (a) The schematic illustration of the tapered optical microfiber modal interferometer based gas sensor. (b) The mode profiles of HE_{11} mode and HE_{12} mode.

Given that I_1 and I_2 are the intensities of HE_{11} mode and HE_{12} mode, respectively; and ϕ is the accumulated phase difference between the two modes after passing through the coupling length L , the output spectrum intensity can thus be modeled as [31]:

$$I = I_1 + I_2 + 2\sqrt{I_1 I_2} \cos \phi \quad (1)$$

The periodic dips on modal interference spectrum are associated with the satisfaction of the following condition:

$$\phi_N = \Delta\beta L = \left(\Delta n_{\text{eff}} \times \frac{2\pi}{\lambda_N} \right) L = (2N - 1)\pi \quad (2)$$

where $\Delta\beta$ and Δn_{eff} are the propagating constant difference and the ERI difference between HE_{11} mode and HE_{12} mode, respectively. λ_N denotes the wavelength of N_{th} dip on the interference spectrum. The RI sensitivity of λ_N can be calculated as [24]:

$$S_{RI} = \left(\frac{\partial \lambda_N}{\partial n} \right) = \frac{\lambda_N}{n_g^{HE11} - n_g^{HE12}} \frac{\partial (\Delta n_{\text{eff}})}{\partial n} = \frac{\lambda_N}{G} \frac{\partial (\Delta n_{\text{eff}})}{\partial n} \quad (3)$$

- where G is the difference between the group ERI of HE_{11} mode, n_g^{HE11} and the group ERI of HE_{12} mode, n_g^{HE12} . The group ERI can be obtained by $n_g = n_{\text{eff}} - \lambda_N \frac{\partial (n_{\text{eff}})}{\partial \lambda_N}$. From Eq. (3), the sensitivity is determined by three terms: wavelength λ_N , G and $\frac{\partial (\Delta n_{\text{eff}})}{\partial n}$. The sensitivity can therefore be greatly enhanced when G approaches 0, i.e. the group effective index of the even mode equals to that of the odd mode. This condition can also be achieved by optimizing the parameters of the tapered optical fibers.

2.2 Numerical analysis of the RI sensitivity around the DTP

First, we carry out numerical analysis to elucidate Eq. (3) and show how the RI sensitivity is influenced by wavelength and group ERI difference, G . Here, we only consider the interference between the two modes in the uniform waist region and neglect the two

nonadiabatic transition regions since they are rather short compared with the waist region [28]. We obtain the ERIs of HE_{11} and HE_{12} modes by numerically solving the Helmholtz equations of optical microfibers [32], then further deduce the values of G and S_{RI} .

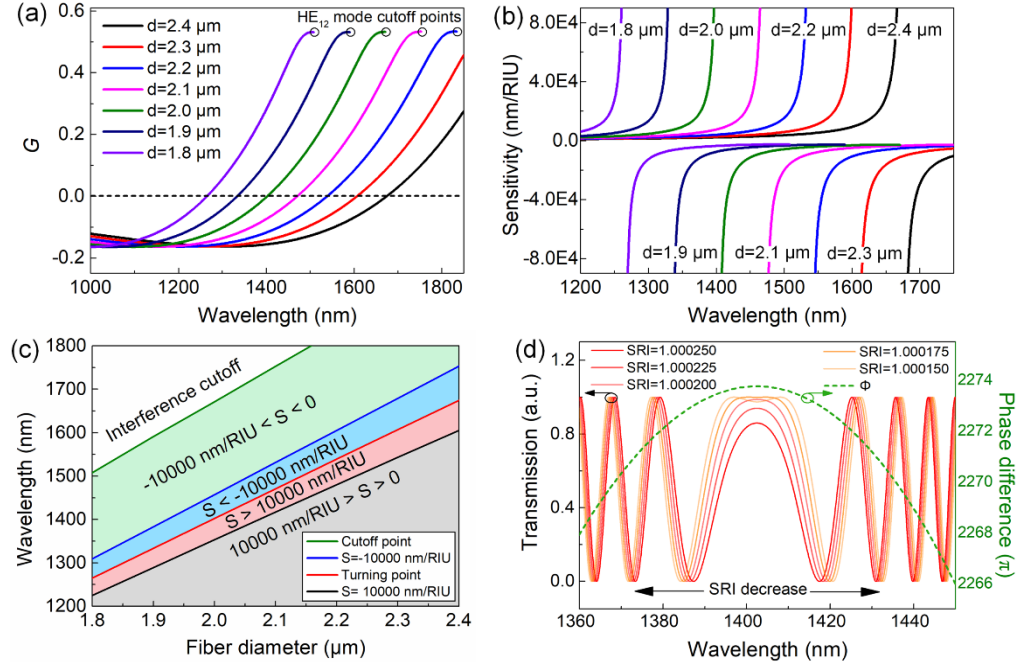


Fig. 2. (a) The G value as a function of wavelength at different waist diameters. (b) The sensitivities around the DTPs at each waist diameter. (c) The high-sensitivity, low-sensitivity and cutoff regions with respect to the DTP. (d) Variation of the interference spectrum of an optical microfiber along with decreasing SRI ($d = 2 \mu m$, $L = 5$ mm).

Figure 2(a) plots the calculated G value as a function of wavelength when the waist diameter is tuned from $1.8 \mu m$ to $2.4 \mu m$. It is shown that the G value experiences the similar evolution along with increasing wavelength (i.e. from $G < 0$ to $G = 0$, and then to $G > 0$) at each diameter. The G value keeps increasing till the reach of HE_{12} mode cutoff wavelength. The DTP is the point where $G = 0$. From Eq. (3) we can deduce that S_{RI} approaches infinity when $G = 0$. Hence RI sensors operating around the DTPs are favored by their outstanding sensitivities. Based on the G values, we calculate S_{RI} as a function of wavelength for each waist diameter, as shown in Fig. 2(b). As expected, S_{RI} approaches $+\infty$ from shorter wavelengths with respect to the DTP and $-\infty$ from longer wavelengths. This is because $\partial(n_{eff})/\partial n$ in Eq. (3) is always negative [23]. As the wavelength drifts away from DTP, the absolute value of S_{RI} rapidly drops and then gradually eases. To obtain a clear picture, we distinguish the high-sensitivity regions and low-sensitivity regions in Fig. 2(c). It can be seen that the high-sensitivity regions with $|S_{RI}| > 10^4$ nm/RIU only span in limited areas around the DTP (the blue and the red areas). This means that the gas sensor should operate within a narrow range of wavelength for each waist diameter in order to achieve the promising sensitivity. Also, we can conclude from the simulation results that the microfiber waist diameter should be controlled in a small range around $2 \mu m$ in order to keep the DTP in the low-loss transmission window (~ 1200 - 1700 nm).

To gain a clearer insight into the RI sensing performance around the DTP, we simulate the transmission spectra of an optical microfiber with a diameter of $2 \mu m$ and a length of 5 mm as

SRI decreases from 1.00025 to 1.00015 with an interval of 0.000025. The spectra are shown in Fig. 2(d). All the spectra show anomalous features different from conventional fiber-optic model interferometers of which the sinusoidal periods are constant. As the wavelength increases from shorter wavelengths to longer wavelengths, the interference period keeps increasing, then broadens and flattens at ~1402 nm, and then decreases dramatically. The wavelength of ~1402 nm is the so-called DTP, and is in good accordance with the numerical results in Fig. 2(a) and (b). The DTP corresponds to the maximum value in phase difference. As SRI decreases, the interference dips/peaks on both sides tend to shift away from the DTP. The closer the dips/peaks are to the DTP, the greater the shifts are. This spectral response is in good agreement with the simulation results in Fig. 2(b).

2.3 Influence of taper length and waist length on DTP

In the above analysis, we only considered the uniform waist region and neglected the tapered regions. We found that the position of the DTP can be tuned by varying the diameter of the microfiber. Here, we study the influences of the taper length and the waist length on the position of the DTP. For the tapered transition regions where the diameter of the fiber varies, Eq. (2)-(3) are not applicable. Here, we adopt a generalized expression to calculate the phase difference between HE_{11} mode and HE_{12} mode accumulated along the tapered regions and the waist region [22].

$$\phi = \int_{-w}^w \Delta\beta dz = \frac{2\pi}{\lambda} \int_{-w}^w \Delta n_{\text{eff}}(z) dz \quad (4)$$

where $z = -w$ and $z = w$ represent the starting point and the end point of the tapered optical fiber. Here $\Delta n_{\text{eff}}(z)$ is the local ERI difference between HE_{11} mode and HE_{12} mode. To numerically calculate the phase difference ϕ , we use a step-like approximation method [33]. We divide the tapered regions into a series of small segments, and replace each tapered segment by a cylindrical segment with the same length and a diameter taken from the middle of the tapered segment. Thus, we can numerically calculate the phase difference accumulated along each small segment via Eq. (2), and obtain the phase difference accumulated along the whole tapered optical fiber through Eq. (4). With the phase difference, we can obtain the output spectrum intensity through Eq. (1).

In our modelling, we adopt an exponential profile [34] to simulate the transition tapers:

$$\rho = \rho_0 \exp(-z / 2L_0) \quad (5)$$

where ρ , ρ_0 and L_0 denote the final diameter, the initial diameter, and the width of the heating region, respectively. We suppose that both the down taper and the up taper have the same profile with a length of L_t , and the length of the waist region to be L_w .

First, we analyze the influence of the taper length L_t on the position of the DTP. Figure 3(a) displays the transmission spectra of tapered optical fibers with taper length varies from 0 to 7 mm ($d = 2 \mu\text{m}$, $L_w = 2 \text{ mm}$, and $\text{SRI} = 1.00025$). When L_t increases, the DTP gradually moves to the longer wavelengths. While the period of interference fringes varies slightly around the DTP. The red-shift of the DTP is attributed to the increase of the relatively thick tapered region, of which the DTP is at longer wavelength. However, the cutoff wavelength of the interference keeps unchanged during the increase of taper length. This is because the cutoff frequency of the HE_{12} mode is governed by the diameter of the waist region, which is the thinnest part of the tapered optical microfiber.

Then, we study the influence of the waist length on the evolution of the DTP. We keep the length of the tapered region to be 3 mm, and vary the length of the waist region from 0.2 mm to 5 mm ($d = 2 \mu\text{m}$ and $\text{SRI} = 1.00025$). Figure 3(b) shows the simulated transmission spectra and the corresponding curves of phase differences. It is interesting to note that when $L_w = 0.2$

mm, the spectrum does not show obvious DTP at the wavelength range of 1200-1670 nm. However, as we increase L_w to 0.5 mm, the DTP appears at a longer wavelength, and moves towards 1400 nm as L_w keeps increasing. The periods of the interference fringes also decrease dramatically along with the increasing of L_w .

The evolution of the spectra indicates that for a tapered optical microfiber with a certain diameter, both the lengths of the tapers and the length of the waist determine the position of the DTP. On one hand, increasing the lengths of the tapered regions will lead to a red-shift to the DTP and even make the DTP shift beyond the cutoff wavelength of the interference if L_t is much larger than L_w . On the other hand, increasing the length of the waist region leads to the blue-shift of DTP and decreases the periods of the interference fringes. Thus, even when the diameter of the waist region falls into the range of 1.8-2.4 μm as predicted in the above section, the length of the waist should be long enough so as to obtain the DTP. Also, for a tapered optical fiber with a waist diameter below 1.8 μm , we can also obtain the DTP in the low-loss transmission window if we properly design the profile of the tapered regions.

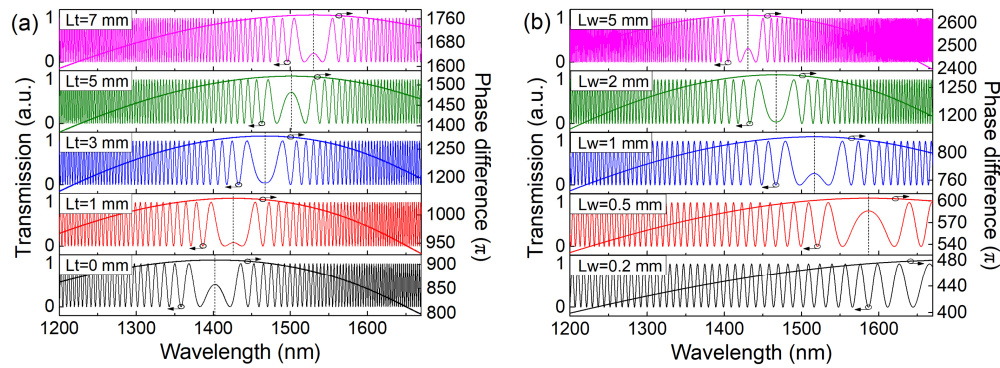


Fig. 3. Calculated transmission spectra and phase differences for tapered optical fibers with different (a) taper length ($d = 2 \mu\text{m}$, $L_w = 2 \text{ mm}$, and $\text{SRI} = 1.00025$) and (b) waist length ($d = 2 \mu\text{m}$, $L_t = 3 \text{ mm}$, and $\text{SRI} = 1.00025$).

3. Experimental results and discussion

The tapered optical microfiber with two abrupt tapers is fabricated by a facile two-step process. Firstly, an SMF is nonadiabatically tapered by a glass processing and splicing machine (LZM-100 LAZERMester). After the first step, the intermediate tapered fiber consists of a $\sim 2 \text{ mm}$ -long waist with a diameter of $\sim 45 \mu\text{m}$ and two abrupt conical taper transitions with lengths of $\sim 1.0 \text{ mm}$. Secondly, the intermediate tapered fiber is further slowly tapered by a flame with a 2 mm-wide heating region. During the second-step tapering, we monitor the real-time transmission spectrum of the fiber using an optical spectrum analyzer (OSA). Once the desirable spectrum appears, we immediately stop the tapering process. Generally, the tapered optical micro/nanofibers are very fragile and difficult to handle. To overcome this problem and enhance the robustness of the tapered fiber, we employ an on-site packaging strategy to fix the tapered fiber into the microchannel of a specially designed aluminum sensor chip on the tapering setup right after fabrication. Then we cover the sensor chip with a piece of surgical mask to prevent dust adsorption onto the microfiber. The aluminum sensor chip together with the tapered fiber are then placed at the bottom of a custom-designed stainless steel vacuum chamber and fixed by double-sided adhesive tapes. There are two small holes on the two opposite side walls of the chamber to allow the lead-in and the lead-out of the SMFs, which are sealed with paraffin once the fibers are positioned. Then we cover the chamber with a rubber ring and a stainless steel cover and seal it tightly with fastened screws. As Fig. 4(a) illustrates, the chamber cover is connected to a vacuum pump and a vacuum meter. The air pressure inside the chamber is controlled by the vacuum pump and the valve. The vacuum value is monitored by the vacuum meter. The input of

microfiber is connected to a broadband light source (BBS) and the transmission spectrum is recorded by an OSA at the output.

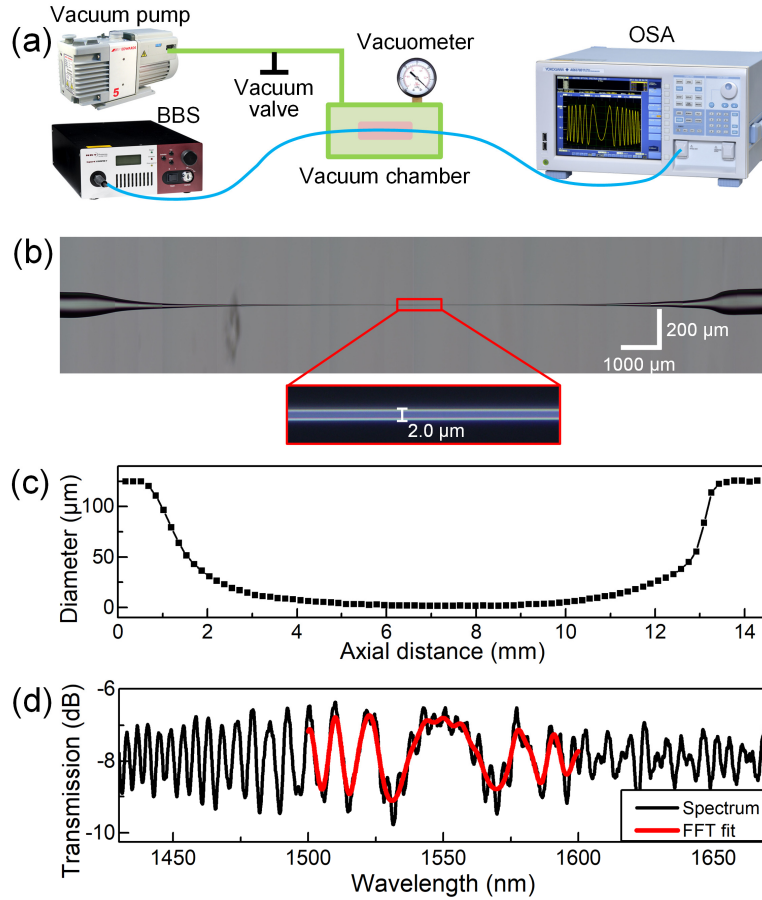


Fig. 4. (a) The experimental setup for gas RI sensing. (b) The microscopic view of the tapered optical microfiber. (c) The diameter variation along the axial direction of the tapered fiber. (d) The original (black) and FFT filtered (red) transmission spectra of the tapered optical microfiber surrounded by air.

Figure 4(b) shows the microscopic view of our fabricated tapered optical microfiber. It has two abrupt tapers and a uniform waist with a diameter of 2.0 μm . We plot the diameter variation along the axial direction of the tapered fiber in Fig. 4(c). It shows that the whole length of the tapered fiber is ~ 13 mm and the waist length is ~ 2.3 mm. The transmission spectrum of the tapered optical microfiber surrounded by air is shown in Fig. 4(d). It is the relative transmission with respect to the transmission of an untapered SMF with the same length. Hence from Fig. 4(d) we can deduce that the optical loss of our fabricated nonadiabatic tapered optical microfiber is 7–9 dB, depending on the wavelength of interest. The sinusoidal modal interference between HE_{11} mode and HE_{12} mode can be clearly identified from shorter wavelengths with respect to the DTP. At longer wavelengths, the sinusoidal interference becomes less obvious due to the cutoff of HE_{12} mode. However, there exist ineffective excitations of higher order modes due to the imperfect structural control during the microfiber fabrication, hence we can still observe some fluctuations at the DTP and longer wavelengths. For a clearer observation of RI sensing performance, we filter out the disturbing

higher order modes from spectrum via fast Fourier Transform (FFT) filtering (the red curve in Fig. 4(d), cutoff frequency: 0.15625).

The change of gas RI inside the chamber is realized via regulating the air pressure. Other factors including temperature and gas composition can also influence the RI of gaseous medium. To eliminate these influences, we carried out the experiments in a cleanroom environment where the temperature (25 ± 0.15 °C) and humidity are kept constant. The relative pressure in the vacuum chamber is adjusted from -50 kPa to 0 with a step of 10 kPa. Figure 5(a) presents the variation of modal interference spectrum around the DTP as the chamber pressure increments. The bold solid lines in Fig. 5(a) are the FFT filtered spectra. As proven by the simulation, the closer the operating wavelength is to the DTP, the higher the S_{ri} is. Therefore, we pick three closest dips from each side of the DTP (a, b, c & a', b', c') as the indicators of chamber pressure as well as RI. The RI is related to the chamber pressure as expressed by Eq. (6):

$$n_{air} = 1 + 7.82 \times 10^{-7} P / (273.6 + T) \quad (6)$$

where n_{air} , P and T represent the RI, the absolute pressure and the temperature of air, respectively. As shown in Fig. 5(a), when the pressure as well as the RI increase, all the dips from both sides shift towards the DTP. Both positive and negative sensitivities are achieved, which match with our simulation results shown in Fig. 2(b).

Figure 5(b) compares the sensitivities of those dips in terms of nm/MPa and nm/RIU. As expected, the twin dips a and a' right next to the DTP provide the highest positive and negative sensitivities, respectively. The other distant dips (b, b', c, and c') are much less sensitive, yet still possess sensitivities higher than 10^4 nm/RIU. All the dips show linear response to pressure and RI variations. The DTP locates at ~ 1550 nm. Our referenced six dips fall within ± 50 nm of the DTP. This is in good agreement with the simulation results in Fig. 2(c) that $|S_{ri}| > 10^4$ nm/RIU can only be achieved within a narrow wavelength range of $\sim \pm 50$ nm with respect to the DTP when the waist diameter is ~ 2 μ m. Another interesting characteristic of RI sensing around the DTP is that tracing the separation between the oppositely drifted twin dips can even double the sensitivity of a single dip. As shown in Fig. 5(c), the distance between twin dips a and a' ($d_{aa'}$) provides a sensitivity as high as -69984.3 ± 2363.3 nm/RIU, which is exceptional in gaseous RI measurements.

We also simulate the transmission spectrum of the tapered fiber using the measured profile as shown in Fig. 4(b) and calculate the sensitivity theoretically. The simulated spectrum is shown in Fig. 5(d), which possesses a DTP at ~ 1540 nm. The simulated spectrum is shown in Fig. 5(d), which possesses a DTP at ~ 1540 nm. There is a ~ 10 nm mismatch between the simulated DTP and the experimental DTP which locates at ~ 1550 nm. This is due to the measurement inaccuracy of the waist diameter under microscope. Based on Fig. 2(a) and (b), we can deduce that the ~ 10 nm mismatch between DTPs corresponds to a deviation of ~ 20 nm in waist diameter measurement. Even so, the simulated spectrum is quite similar to the measured spectrum shown in Fig. 5(a). The simulated sensitivity curves also have very similar trends with the experimental results [Fig. 5(e)], indicating the reliability of our theoretical model.

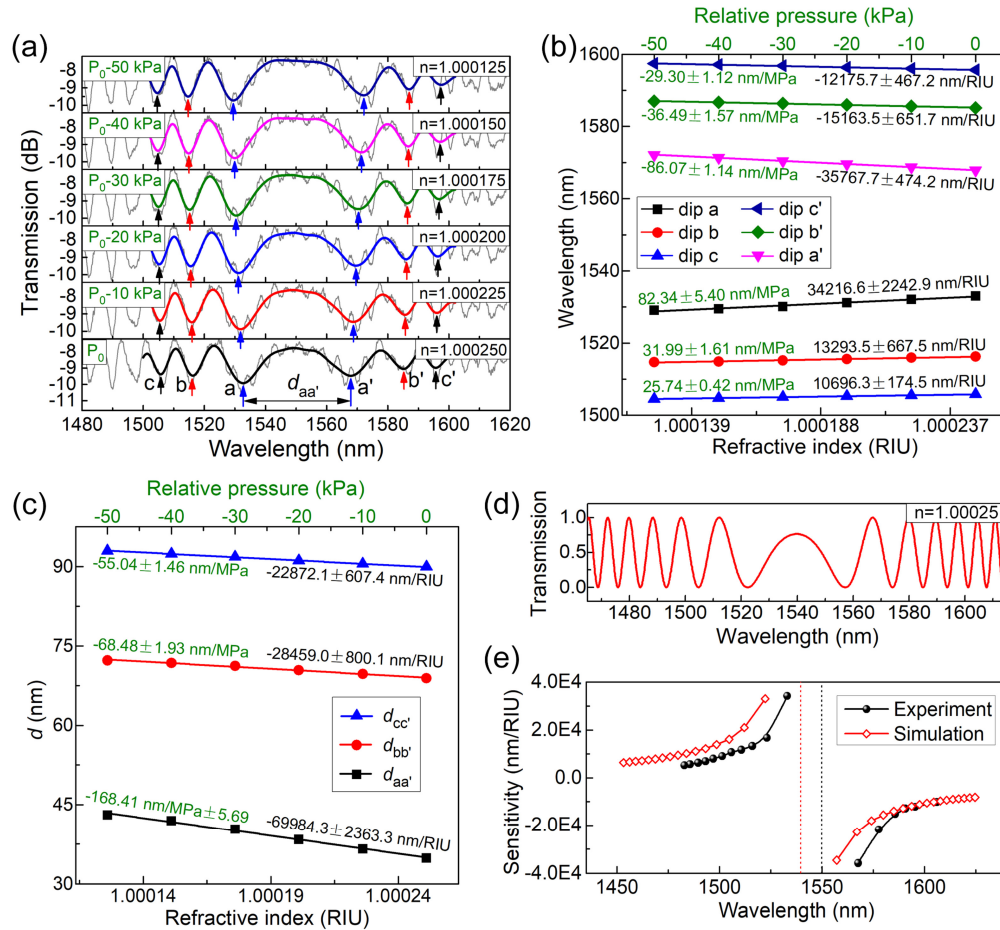


Fig. 5. (a) The variation of the interference spectrum along with decremented air pressure and SRI. (b) The linear sensitivities of the six dips around the DTP. (c) The doubled sensitivities by tracing the distance between oppositely drifted twin dips. (d) The simulated spectrum using the measured profile of the tapered optical fiber. (e) Comparison of the sensitivities of the dips and peaks around the DTP between the measured results and the simulated results.

To verify the stability and accuracy of the proposed gas RI sensor, the influence of temperature on the sensor is also studied. We place the gas sensing platform into a commercial customized thermostat chamber and gradually increase the temperature from room temperature (25.0 °C) to 32.0 °C with a step of 1.0 °C. Figure 6(a) plots the resultant spectra which show slight blue-shift for dip a, b and c and slight red-shift for dip a', b' and c' as temperature rises. The wavelengths of the interference dips with temperature variations are displayed in Fig. 6(b), where good linear responses of the six dips are obtained. Similar with the RI sensing, the twin dips closest to the DTP (a and a') are the most sensitive to the temperature change and their sensitivities are -2.134 ± 0.079 nm/°C and 1.899 ± 0.054 nm/°C, respectively. Certainly, the distances between twin dips provide doubled temperature responses [Fig. 6(c)]. The temperature responses are mainly caused by the thermal-optical effects of both the microfiber and the air. Even though the cross sensitivity is relatively higher than those of conventional fiber optic gas sensors, its influence on the practical use is negligible compared with the ultrahigh RI sensitivity.

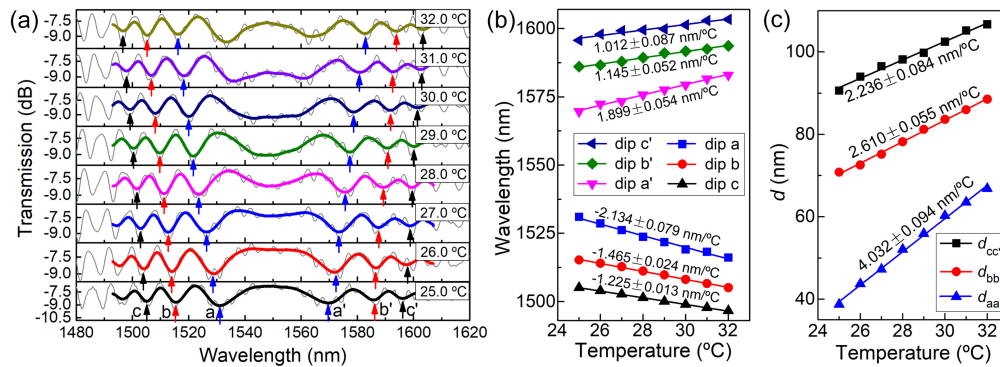


Fig. 6. (a) The variation of modal interference spectrum along with incremented temperature from 25.0 °C to 32.0 °C. (b) The temperature sensitivities of the referenced six dips. (c) The doubled temperature sensitivities by tracing the distance between twin dips.

4. Conclusions

We demonstrate an ultrasensitive gas sensor based on tapered optical microfiber modal interferometer operating at the DTP. We theoretically investigate how the structural parameters including waist diameter, waist length and taper length of the tapered optical microfiber influence the spectral characteristics at DTP. We also numerically prove that the ultrahigh RI sensitivities can be achieved within a narrow wavelength range of ± 50 nm with respect to the DTP, and the proper microfiber waist diameter is ~ 2 μm . Our experimental demonstration verifies the simulation results and achieves a sensitivity of gaseous RI (~ 1.0) as high as $-69984.3 \pm 2363.3 \text{ nm/RIU}$.

Funding

Singapore Ministry of Education Academic Research Fund Tier 2 (MOE2015-T2-1-066 and MOE2015-T2-2-010); Singapore Ministry of Education Academic Research Fund Tier 1 (RG85/16); Nanyang Technological University (Start-up grant M4081515: Lei Wei).

References

1. A. Sampaolo, P. Patimisco, M. Giglio, L. Chieco, G. Scamarcio, F. K. Tittel, and V. Spagnolo, "Highly sensitive gas leak detector based on a quartz-enhanced photoacoustic SF₆ sensor," *Opt. Express* **24**(14), 15872–15881 (2016).
2. S. Asaduzzaman and K. Ahmed, "Proposal of a gas sensor with high sensitivity, birefringence and nonlinearity for air pollution monitoring," *Sens. Biosensing Res.* **10**, 20–26 (2016).
3. N. Shehata, G. Brönstrup, K. Funka, S. Christiansen, M. Leja, and H. Haick, "Ultrasensitive silicon nanowire for real-world gas sensing: noninvasive diagnosis of cancer from breath volatolome," *Nano Lett.* **15**(2), 1288–1295 (2015).
4. M.-K. Bae, J. A. Lim, S. Kim, and Y.-W. Song, "Ultra-highly sensitive optical gas sensors based on chemomechanical polymer-incorporated fiber interferometer," *Opt. Express* **21**(2), 2018–2023 (2013).
5. Y. Wu, B. Yao, C. Yu, and Y. Rao, "Optical graphene gas sensors based on microfibers: A review," *Sensors (Basel)* **18**(4), 941 (2018).
6. J. Hodgkinson and R. P. Tatam, "Optical gas sensing: A review," *Meas. Sci. Technol.* **24**(1), 012004 (2013).
7. W. Jin, H. L. Ho, Y. C. Cao, J. Ju, and L. F. Qi, "Gas detection with micro- and nano-engineered optical fibers," *Opt. Fiber Technol.* **19**(6), 741–759 (2013).
8. F. Tian, J. Kanka, and H. Du, "Long-period grating and its cascaded counterpart in photonic crystal fiber for gas phase measurement," *Opt. Express* **20**(19), 20951–20961 (2012).
9. L. Wei, T. T. Alkeskjold, and A. Bjarklev, "Tunable and rotatable polarization controller using photonic crystal fiber filled with liquid crystal," *Appl. Phys. Lett.* **96**(24), 241104 (2010).
10. N. Zhang, G. Humbert, T. Gong, P. Shum, K. Li, J. Auguste, Z. Wu, J. Hu, F. Luan, Q. X. Dinh, M. Olivo, and L. Wei, "Side-channel photonic crystal fiber for surface enhanced Raman scattering sensing," *Sen. Actuators B Chem.* **223**, 195–201 (2016).
11. N. Zhang, G. Humbert, Z. Wu, K. Li, P. P. Shum, N. M. Zhang, Y. Cui, J. L. Auguste, X. Q. Dinh, and L. Wei, "In-line optofluidic refractive index sensing in a side-channel photonic crystal fiber," *Opt. Express* **24**(24), 27674–27682 (2016).

12. M. Zhang, K. Li, T. Zhang, P. Shum, Z. Wang, Z. Wang, N. Zhang, J. Zhang, T. Wu, and L. Wei, "Electron-rich two-dimensional molybdenum trioxides for highly integrated plasmonic biosensing," *ACS Photonics* **5**(2), 347–352 (2018).
13. N. Zhang, K. Li, Y. Cui, Z. Wu, P. P. Shum, J. L. Auguste, X. Q. Dinh, G. Humbert, and L. Wei, "Ultra-sensitive chemical and biological analysis via specialty fibers with built-in microstructured optofluidic channels," *Lab Chip* **18**(4), 655–661 (2018).
14. C. Hou, X. Jia, L. Wei, A. M. Stolyarov, O. Shapira, J. D. Joannopoulos, and Y. Fink, "Direct atomic-level observation and chemical analysis of ZnSe synthesized by in situ high-throughput reactive fiber drawing," *Nano Lett.* **13**(3), 975–979 (2013).
15. S. Shabahang, G. Tao, J. J. Kaufman, Y. Qiao, L. Wei, T. Bouchenet, A. P. Gordon, Y. Fink, Y. Bai, R. S. Hoy, and A. F. Abouraddy, "Controlled fragmentation of multimaterial fibres and films via polymer cold-drawing," *Nature* **534**(7608), 529–533 (2016).
16. T. Zhang, K. Li, J. Zhang, M. Chen, Z. Wang, S. Ma, N. Zhang, and L. Wei, "High-performance, flexible, and ultralong crystalline thermoelectric fibers," *Nano Energy* **41**, 35–42 (2017).
17. J. Zhang, K. Li, T. Zhang, P. J. Buenconsejo, M. Chen, Z. Wang, M. Zhang, Z. Wang, and L. Wei, "Laser induced in-fiber fluid dynamical instabilities for precise and scalable fabrication of spherical particles," *Adv. Funct. Mater.* **27**(43), 1703245 (2017).
18. K. Li, N. Zhang, N. M. Y. Zhang, G. Liu, T. Zhang, and L. Wei, "Ultrasensitive measurement of gas refractive index using an optical nanofiber coupler," *Opt. Lett.* **43**(4), 679–682 (2018).
19. J. Wu, M. Yao, F. Xiong, A. Ping Zhang, H. Y. Tam, and P. K. A. Wai, "Optical Fiber-Tip Fabry-Pérot Interferometric Pressure Sensor Based on an in Situ μ -Printed Air Cavity," *J. Light. Technol.* **36**(17) 3618–3623 (2018).
20. N. L. P. Andrews, R. Ross, D. Munzke, C. van Hoorn, A. Brzezinski, J. A. Barnes, O. Reich, and H.-P. Loock, "In-fiber Mach-Zehnder interferometer for gas refractive index measurements based on a hollow-core photonic crystal fiber," *Opt. Express* **24**(13), 14086–14099 (2016).
21. M. Quan, J. Tian, and Y. Yao, "Ultra-high sensitivity Fabry-Perot interferometer gas refractive index fiber sensor based on photonic crystal fiber and Vernier effect," *Opt. Lett.* **40**(21), 4891–4894 (2015).
22. S. Lacroix, F. Gonthier, R. J. Black, and J. Bures, "Tapered-fiber interferometric wavelength response: the achromatic fringe," *Opt. Lett.* **13**(5), 395–397 (1988).
23. P. Pilla, C. Trono, F. Baldini, F. Chiavaioli, M. Giordano, and A. Cusano, "Giant sensitivity of long period gratings in transition mode near the dispersion turning point: an integrated design approach," *Opt. Lett.* **37**(19), 4152–4154 (2012).
24. X. Shu, L. Zhang, and I. Bennion, "Sensitivity characteristics near the dispersion turning points of long-period fiber gratings in B/Ge codoped fiber," *Opt. Lett.* **26**(22), 1755–1757 (2001).
25. C. Lu, X. Dong, and J. Su, "Detection of Refractive Index Change from the Critical Wavelength of an Etched Few Mode Fiber," *J. Lit. Technol.* **35**(13), 2593–2597 (2017).
26. E. Salik, M. Medrano, G. Cohoon, J. Miller, C. Boyter, and J. Koh, "SMS fiber sensor utilizing a few-mode fiber exhibits critical wavelength behavior," *IEEE Photonics Technol. Lett.* **24**(7), 593–595 (2012).
27. J. Su, X. Dong, and C. Lu, "Intensity detection scheme of sensors based on the modal interference effect of few mode fiber," *Measurement* **79**, 182–187 (2016).
28. H. Luo, Q. Sun, X. Li, Z. Yan, Y. Li, D. Liu, and L. Zhang, "Refractive index sensitivity characteristics near the dispersion turning point of the multimode microfiber-based Mach-Zehnder interferometer," *Opt. Lett.* **40**(21), 5042–5045 (2015).
29. K. Li, N. M. Y. Zhang, N. Zhang, T. Zhang, G. Liu, and L. Wei, "Spectral Characteristics and Ultrahigh Sensitivities Near the Dispersion Turning Point of Optical Microfiber Couplers," *J. Lit. Technol.* **36**(12), 2409–2415 (2018).
30. K. Li, T. Zhang, G. Liu, N. Zhang, M. Zhang, and L. Wei, "Ultrasensitive optical microfiber coupler based sensors operating near the turning point of effective group index difference," *Appl. Phys. Lett.* **109**(10), 101101 (2016).
31. W. B. Ji, Y. C. Tan, B. Lin, S. C. Tjin, and K. K. Chow, "Nonadiabatically tapered microfiber sensor with ultrashort waist," *IEEE Photonics Technol. Lett.* **26**(22), 2303–2306 (2014).
32. L. Tong, J. Lou, and E. Mazur, "Single-mode guiding properties of subwavelength-diameter silica and silicon wire waveguides," *Opt. Express* **12**(6), 1025–1035 (2004).
33. S. W. Yang, T. L. Wu, C. W. Wu, and H. C. Chang, "Numerical modeling of weakly fused fiber-optic polarization beamsplitters - Part II: The three-dimensional electromagnetic model," *J. Lit. Technol.* **16**(4), 691–696 (1998).
34. J. Villatoro, D. Monzón-Hernández, and E. Mejía, "Fabrication and modeling of uniform-waist single-mode tapered optical fiber sensors," *Appl. Opt.* **42**(13), 2278–2283 (2003).